CrossMark

ARTICLE

Heterostructured $ZnFe_2O_4$/Fe_2TiO_5/TiO_2 Composite Nanotube Arrays with an Improved Photocatalysis Degradation Efficiency Under Simulated Sunlight Irradiation

Kun Xiong[1] · Kunzhou Wang[1] · Lin Chen[1] · Xinqing Wang[1] ·
Qingbo Fan[1] · Jérémie Courtois[1] · Yuliang Liu[1] ·
Xianguo Tuo[2] · Minhao Yan[1]

Highlights

- $ZnFe_2O_4$ nanocrystals were perfused into pristine TiO_2 nanotube array pipelines using a novel bias voltage-assisted perfusion method.
- Novel heterostructured $ZnFe_2O_4$/Fe_2TiO_5/TiO_2 composite nanotube arrays were obtained with staggered type II band alignment at the $ZnFe_2O_4$/Fe_2TiO_5 interface and type I band alignment at the Fe_2TiO_5/TiO_2 interface.
- Visible light absorption and the photocatalytic degradation efficiency of methylene blue were significantly improved upon irradiation with simulated sunlight.

Abstract To improve the visible light absorption and photocatalytic activity of titanium dioxide nanotube arrays (TONTAs), $ZnFe_2O_4$ (ZFO) nanocrystals were perfused into pristine TONTA pipelines using a novel bias voltage-assisted perfusion method. ZFO nanocrystals were well anchored on the inner walls of the pristine TONTAs when the ZFO suspensions (0.025 mg mL^{-1}) were kept under a 60 V bias voltage for 1 h. After annealing at 750 °C for 2 h, the heterostructured ZFO/Fe_2TiO_5 (FTO)/TiO_2 composite nanotube arrays were successfully obtained. Furthermore, Fe^{3+} was reduced to Fe^{2+} when solid solution reactions occurred at the interface of ZFO and the pristine TONTAs. Introducing ZFO significantly enhanced the
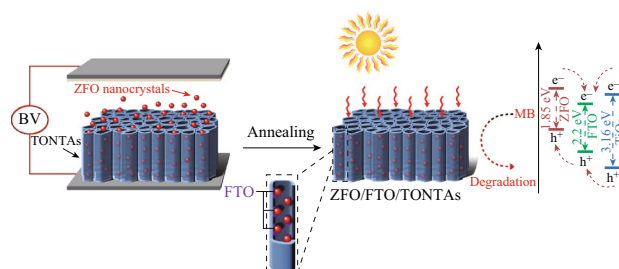
visible light absorption of the ZFO/FTO/TONTAs relative to that of the annealed TONTAs. The coexistence of type I and staggered type II band alignment in the ZFO/FTO/TONTAs facilitated the separation of photogenerated electrons and holes, thereby improving the efficiency of the ZFO/FTO/TONTAs for photocatalytic degradation of methylene blue when irradiated with simulated sunlight.

Kun Xiong and Kunzhou Wang have contributed equally to this work.

✉ Xianguo Tuo
tuoxianguo@suse.edu.cn

✉ Minhao Yan
yanminhao@swust.edu.cn

1 State Key Laboratory Cultivation Base for Nonmetal Composites and Functional Materials, Southwest University of Science and Technology, Mianyang 621010, People's Republic of China

2 Sichuan University of Science and Engineering, Zigong 643000, People's Republic of China

🅶 Springer

1 Introduction

Semiconductor photocatalysts have attracted considerable research interests because of their potential value in environmental remediation [1–5]. As an excellent UV light-driven photocatalyst, nano-TiO_2 powders are already commercially available (Evonik Degussa P25). Recently, TiO_2 nanotube arrays (TONTAs) were found to possess superior electron percolation pathways for charge transfer than randomly arranged TiO_2 nanocrystals, which is probably due to their unique structural arrangement [6, 7]. Therefore, TONTAs have been widely investigated for hydrogen production via water splitting [8–10], photocatalytic degradation of organic pollutants [11–13], dye-sensitized solar cells [14–17], and photoelectrodes [18–20]. However, because of the wide bandgap of TiO_2 (3.2 eV for anatase; 3.0 eV for rutile), it absorbs light in the UV region, which only occupies 4–5% of the total solar spectrum. This results in lower solar energy utilization [21]. Therefore, many methods have been investigated to improve the visible light absorption of TONTAs.

Visible light absorption by TONTAs can be enhanced by metal (Ag [22], Au [23, 24], and Pd [25]) and nonmetal (N [26, 27], C [28, 29], F [30–32], and B [33, 34]) doping, but this approach remains challenging because of carrier recombination centers. Based on heterojunction energy band theory, the recombination of photogenerated electrons and holes can be effectively reduced when a staggered type II band alignment is formed at the interface of TONTAs and narrow bandgap semiconductors (such as CdS [35–37], CdSe [38, 39], RuO_2 [40, 41], and NiO [42, 43]).

In recent years, $ZnFe_2O_4$ (ZFO) has attracted considerable attention because of its narrow bandgap (1.86 eV), which can help it to harvest approximately 46% of sunlight [44, 45]. In contrast to pure TiO_2 nanoparticles, ZFO/TiO_2 composite nanoparticles exhibited a better activity in the photodegradation of methyl orange, but their energy conversion efficiency remained relatively low [46]. Furthermore, the visible light-induced photocatalytic activity could be further enhanced when ZFO nanocrystals were anchored on the inner walls of the TONTAs [21]. Additionally, the ZFO/TONTA composite was investigated and required no sacrificial agent to consume the photogenerated electrons. Charge carriers that were excited from TiO_2 and were transferred to ZFO could recombine, which lowered the photocatalytic efficiency for the degradation of methyl orange [47]. Similar effects were found when $BiFeO_3$ nanocrystals were anchored on the inner walls of TONTAs. Sarkar et al. [48] found that these heterostructures facilitated separation of photogenerated electrons and holes to form more hydroxyl radicals ($\cdot$OH). Zhu et al. [49] reported that lattice-matched pseudobrookite (Fe_2TiO_5, FTO) could

be grown on the surface of TiO_2 via solid-state reactions between Fe_2O_3 and TiO_2. In contrast to TiO_2, FTO has a relatively narrow bandgap (2.2 eV) [50]. Liu et al. [51] prepared an ultrathin FTO layer on the inner walls of TONTAs and showed that visible light absorption of the FTO/TiO_2 composite nanotube arrays and the associated energy conversion efficiency were significantly improved.

Herein, we describe a novel heterostructured ZFO/FTO/TiO_2 composite nanotube array (ZFO/FTO/TONTAs). No studies have yet reported the preparation of ZFO/FTO/TONTAs or their photocatalytic performances. In this work, ZFO nanocrystals were first perfused into pristine TONTA pipelines using a bias voltage. They were then annealed to form ZFO/FTO/TONTAs. The phase composition, microstructure, and photocatalytic performance of ZFO/FTO/TONTAs were investigated, and the photocatalytic enhancement mechanism was also discussed.

2 Experimental Section

2.1 Synthesis of TONTAs and ZFO Nanocrystals

TONTAs were prepared using the electrochemical anodization method. Prior to anodization, the commercially purchased Ti foils ($40 \times 50 \times 1$ mm^3, purity > 99.5%) were physically and chemically polished. The Ti foils were anodized in a two-electrode cell, and Pt-plated Ti (Pt/Ti) foil was used as the cathode. The electrolyte was composed of 1.5 wt% ammonium fluoride, 91 vol% ethylene glycol, and 9 vol% deionized (DI) water. When the anodization voltage was held at 60 V for 2 h, the largest TONTAs (diameter $\approx$ 180 nm) were obtained.

The hydrothermal method was used to prepare ZFO nanocrystals, as described in our previous study [52]. Briefly, $Zn(NO_3)_2 \cdot 6H_2O$ (Sigma-Aldrich) and $Fe(NO_3)_3 \cdot 9H_2O$ (Sigma-Aldrich) were completely dissolved in 60 mL of DI water, corresponding to final concentrations of 20 and 40 mM, respectively. The pH value was adjusted to 10 by dropwise addition of an ammonia solution (25 wt%) to obtain a well-dispersed brown dispersion. The samples were transferred into a 100-mL Teflon autoclave, sealed, and heated at 170 °C for 6 h. Then, the brown precipitates were collected and transferred to a new beaker. The obtained products were carefully rinsed three times with DI water.

To minimize soft aggregation of ZFO nanocrystals, concentrated nitric acid (60 wt%) and DI water were added at a volume ratio of 1:3 and stirred with a magnetic stirrer. This process was repeated three times. The stirring times were 30 (first time), 20 (second time), and 10 min (third time). A magnet was used to deposit the as-prepared ZFO nanocrystals on the bottom of the beaker, and the

supernatant liquid was removed. With magnetic stirring, the ZFO nanocrystals were washed with acetone for 30 min to remove the residual nitrate ions and were re-dispersed in DI water to obtain a bright brown liquid with a ZFO concentration of 0.75 mg mL^{-1}.

2.2 Preparation of ZnFe$_2$O$_4$/Fe$_2$TiO$_5$/TiO$_2$ Composite Nanotube Arrays

A novel bias voltage-assisted perfusion method was used to anchor the as-prepared ZFO nanocrystals on the inner walls of the pristine TONTAs (as shown in Fig. 1). The TONTA/Ti foil and Pt/Ti foil were separately used as the cathode and anode, respectively. The ZFO nanocrystals were well perfused into pristine TONTA pipelines under a 60-V direct current bias voltage. The perfusion time and concentration of ZFO nanocrystals were 1 h and 0.025 mg mL^{-1}, respectively. When the perfusion process was finished, the TONTA/Ti foil was repeatedly rinsed with DI water and air-dried. They were subsequently transferred into a furnace and annealed under varying temperatures (650, 750, and 850 °C) for 2 h in air. Finally, a blade was used to remove the as-prepared ZFO/FTO/TONTAs from the Ti foil.

2.3 Characterization of the Samples

The phase composition of the samples was characterized by X-ray diffraction (XRD, X'Pert PRO, PANalytical, the Netherlands) using a Cu $K\alpha$ source ($\lambda = 1.5406$ Å). The morphology of the samples was observed using field emission scanning electron microscopy (FE-SEM, ZEISS Ultra 55, Germany) and high-resolution transmission electron microscopy (HR-TEM, LIBRA 200FE, ZEISS, Germany). The chemical compositions of the samples were determined by X-ray photoelectron spectroscopy (XPS, XSAM 800, Kratos, UK), and the binding energies were normalized to the signal for adventitious C1s at 284.8 eV.

The hydrodynamic diameter (D_H) of the as-prepared ZFO nanocrystals in dispersion was monitored by a

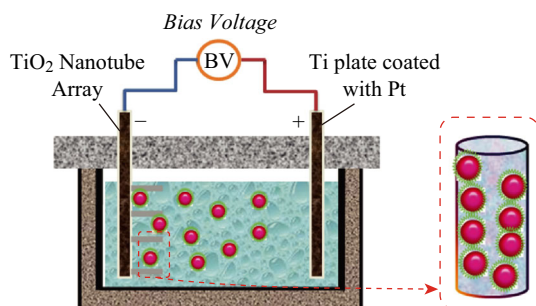**Fig. 1** Schematic representation of the bias voltage-assisted perfusion process

dynamic light scattering (DLS) technique using a multi-angle particle size and zeta potential analyzer (Brookhaven NanoBrook Omni, USA). The specific surface areas were determined using the Brunauer–Emmett–Teller (BET) method with a Quantachrome NOVA 3000 Analyzer (USA). The UV–Vis diffuse reflection measurements used a UV–V is (NIR) spectrophotometer (SolidSpec-3700, Shimadzu, Japan). Photoluminescence (PL) measurements were carried out at room temperature using a fluorescence spectrometer (PerkinElmer, LS55, USA) with a xenon lamp as the excitation source ($\lambda_{ex} = 370$ nm).

2.4 Photocatalytic Activity Measurement

The photocatalytic activity of the samples was investigated by measuring the degradation of methylene blue (MB) in an aqueous solution under simulated sunlight. The light source was a 300-W xenon lamp (PLS-SXE300; 320–780 nm), and the operating current was kept at 15 A. The photon intensity used during photocatalytic activity measurements was 2000 mW cm^{-2} and 10 cm from the outlet of the light source. In this work, 50 mg of pure ZFO nanocrystals, TONTAs (annealed at 600 °C), and ZFO/FTO/TONTAs (annealed at 750 °C) were separately added to 100 mL of an MB aqueous solution (10 mg L^{-1}). These suspensions were magnetically stirred for 30 min in the dark to reach absorption–desorption equilibrium, and the MB solution was then replenished to maintain its initial concentration at 10 mg mL^{-1}. Subsequently, the suspensions were irradiated under simulated sunlight, and 4-mL aliquots of the suspensions were collected at predetermined intervals (10, 20, 30, 40, 60, 90, 120, and 150 min). The suspensions were centrifuged at 12,000 rpm for 5 min to remove the solid residues, and the concentration of MB molecules in the supernatant was determined by absorbance at 665 nm in the UV–VIS absorption spectrum (UV-1800, Shimadzu, Japan). During photocatalytic MB degradation, the temperature of the sample was kept constant at 25 °C by circulating water.

2.5 Photoelectrochemical Measurement

Photocurrent measurements were carried out in a quartz beaker using an electrochemical workstation (PGSTAT302, Metrohm, Switzerland) in a standard three-electrode configuration with TONTAs and ZFO/FTO/TONTAs as the working electrodes. The counter and reference electrodes were a Pt wire and saturated calomel electrode, respectively. A 0.1 M Na$_2$SiO$_4$ aqueous solution was used as the electrolyte. The areas of the working electrodes were 12 cm^2. The working electrode was irradiated with a xenon lamp during the measurements. The distance between the window of the flask and light source

was 20 cm. The focused incident light intensity on the flask was ~ 100 mW cm^{-2}.

3 Results and Discussion

Figure 2a shows that the pristine TONTAs are highly ordered and compactly arranged. The nanotubes are well attached to each other, and the average tube diameter is about 180 nm. The cross-sectional image further illustrates that the pristine TONTAs have a highly oriented structure (Fig. 2b). The nanotubes are straight and cylindrical with an estimated length of 1.8–2.0 μm. The TEM image shows that the diameters of the as-prepared ZFO nanocrystals range from 7 to 15 nm (Fig. 2c), whereas the DLS experiment indicates that D_H is approximately 35 nm (inset of Fig. 2c). This suggests that weak particle aggregation may

exist. Nevertheless, the D_H of the as-prepared ZFO nanocrystals remains far smaller than the tube diameter of the TONTAs. In fact, Fig. 2d demonstrates that the ZFO nanocrystals could be well perfused into the nanotubes with only a few clogging incidents at the entrance of the nanotubes. Moreover, the gaps between the TiO$_2$ nanotubes are filled by ZFO nanocrystals.

The TEM images of the TONTAs before (Fig. 2a, e) and after (Fig. 2c, i) the perfusion of ZFO nanocrystals show that the inner walls of the TONTAs become covered with ZFO nanocrystals, including both extremities and the central area of the nanotubes. This explains why some of the ZFO nanoparticles are observed outside of the nanotubes. After annealing at 750 °C for 2 h, the cross-sectional SEM image shows that the previously smooth walls of the tubes become uneven, which originates from the
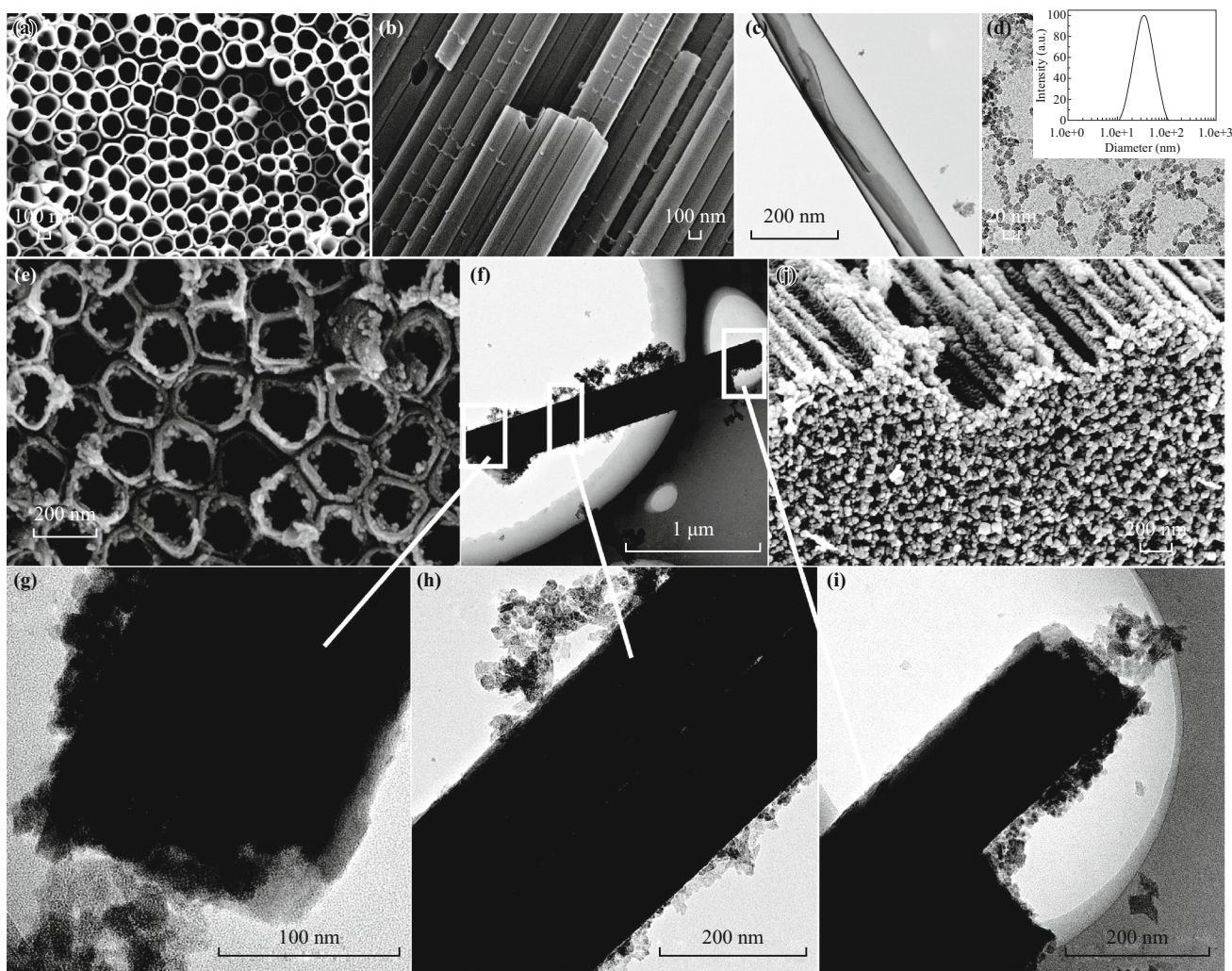
Fig. 2 **a** SEM images of the surface morphology and **b** the cross-sectional morphology of the pristine TONTAs. TEM images of the pristine TONTAs **c** and the ZFO nanocrystals **d** (The inset is DLS spectrum of the ZFO nanocrystals). **e** SEM image and **f** TEM image of the pristine ZFO/TONTAs. **g** The left extremity, **h** central part, and **i** right extremity of Fig. **f**. **j** SEM image of the ZFO/FTO/TONTAs annealed at 750 °C

crystallization of TiO_2 during annealing (Fig. 2j). The annealed tubes reserve their initial linear arrangement.

For the as-prepared composite nanotube arrays annealed at 650 °C, anatase TiO_2 (JCPDS card No. 00-021-1272), rutile TiO_2 (JCPDS card No. 00-021-1276), and ZFO (JCPDS card No. 00-022-1012) are identified. At 750 °C, in addition to anatase TiO_2, rutile TiO_2, and ZFO, diffraction peaks of FTO (JCPDS card No. 01-073-1898) are also observed (Fig. 3a). This demonstrates that the ZFO/FTO/TONTAs were successfully prepared. At 850 °C, anatase TiO_2 transforms into rutile TiO_2 (Fig. 3b), while more FTO (JCPDS card No. 00-003-0374) forms at the ZFO/TiO_2 interface. This suggests that the increase in annealing temperature could promote solid solution reactions. While the anatase phase of TiO_2 has a higher Fermi level, it also has a lower capacity to absorb oxygen and higher degree of hydroxylation. Thus, it possesses a better photocatalytic activity than rutile TiO_2 [53]. Nevertheless, a mixture of anatase and rutile is more active than pure anatase [54], including Degussa P25, which is a commercial TiO_2 photocatalyst. The ZFO/FTO/TONTAs annealed at 750 °C were used for subsequent studies.

Figure 4a shows the XPS survey spectrum of the TONTAs and clearly indicates the presence of all constituent elements, including Ti and O; the C 1s peak is ascribed to carbon from the environment. In addition to the peaks corresponding to Ti 2p and O 1s, Zn 2p and Fe 2p peaks are found in the XPS survey spectrum of the ZFO/FTO/TONTAs. By observing the 2p core level XPS spectra of Ti, the peaks situated at 464.04 and 458.38 eV should be accordingly assigned to Ti $2p_{1/2}$ and Ti $2p_{3/2}$, implying the presence of tetravalent Ti (Ti^{4+}) in the TONTAs (Fig. 4b) [48, 55, 56]. However, for the ZFO/FTO/TONTAs, the binding energies of Ti $2p_{1/2}$ and Ti $2p_{3/2}$ are 463.84 and 458.24 eV (Fig. 4c), respectively, suggesting that the Ti 2p peaks slightly shift toward lower binding energies, unlike those of the TONTAs. This is attributed to the presence of FTO in the ZFO/FTO/TONTAs. Furthermore, there is no evidence of trivalent Ti (Ti^{3+}), which usually appears at 457.4 eV [57].

As presented in Fig. 4d, the Fe 2p core level XPS spectrum of the ZFO/FTO/TONTAs can be fitted with six peaks. These peaks are situated at 709.7 and 723.05 eV and represent the +2 oxidation state of iron (Fe^{2+}). The peaks at 711.68 and 726.01 eV are assigned to trivalent iron (Fe^{3+}). The peaks at 714.86 and 719.13 eV correspond to Fe^{2+} and Fe^{3+} satellite signals, respectively [21, 58, 59]. No Fe^{2+} is observed in the raw materials.

Frandsen et al. [60] reported that Fe^{3+} could be reduced to Fe^{2+} when Ti^{4+} was substituted for Fe^{3+} ($2Fe^{3+} \rightarrow Fe^{2+} + Ti^{4+}$). Therefore, the solid solution reactions that occur at the interface of ZFO and the pristine TONTAs form Fe^{2+}. The Zn 2p core level XPS spectrum is shown in
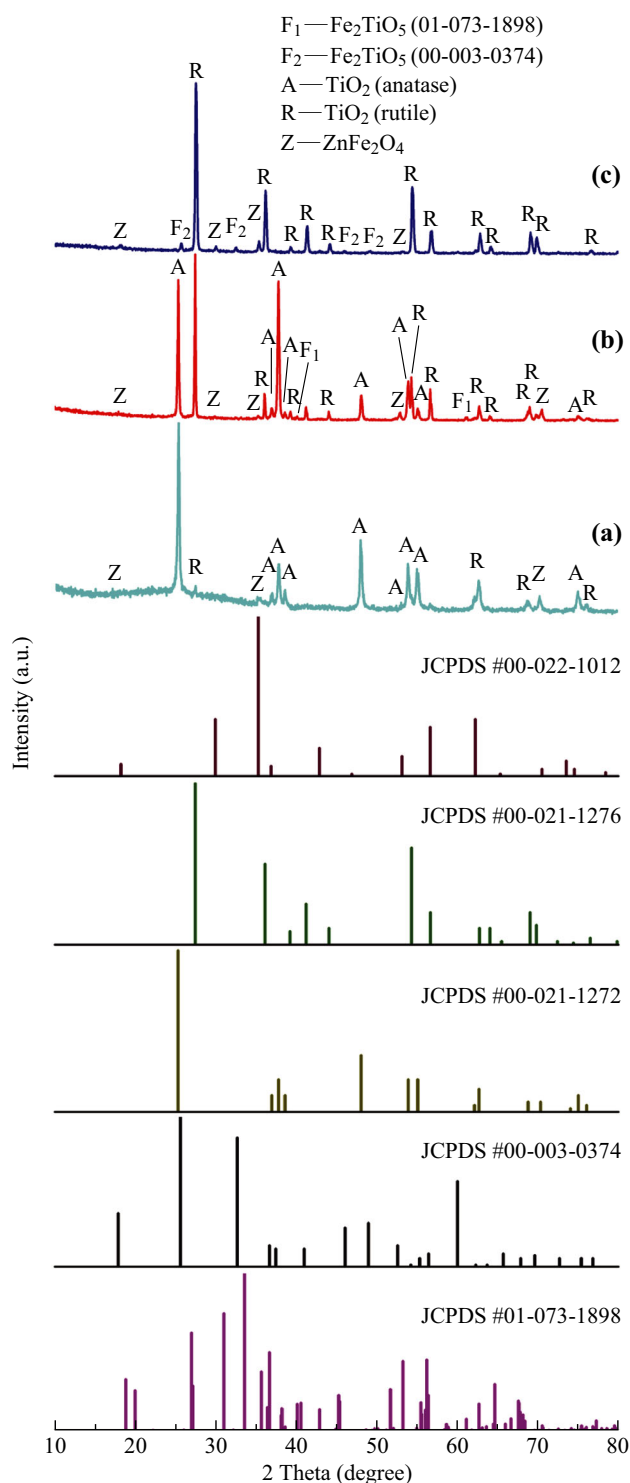
Fig. 3 XRD patterns of the ZFO/FTO/TONTAs annealed at **a** 650 °C, **b** 750 °C, and **c** 850 °C

Fig. 4e. The peaks situated at 1044.13 and 1021.04 eV are assigned to Zn $2p_{1/2}$ and Zn $2p_{3/2}$, implying the presence of bivalent Zn in the ZFO/FTO/TONTAs [61]. Furthermore, the O 1s core level XPS spectrum of the ZFO/FTO/
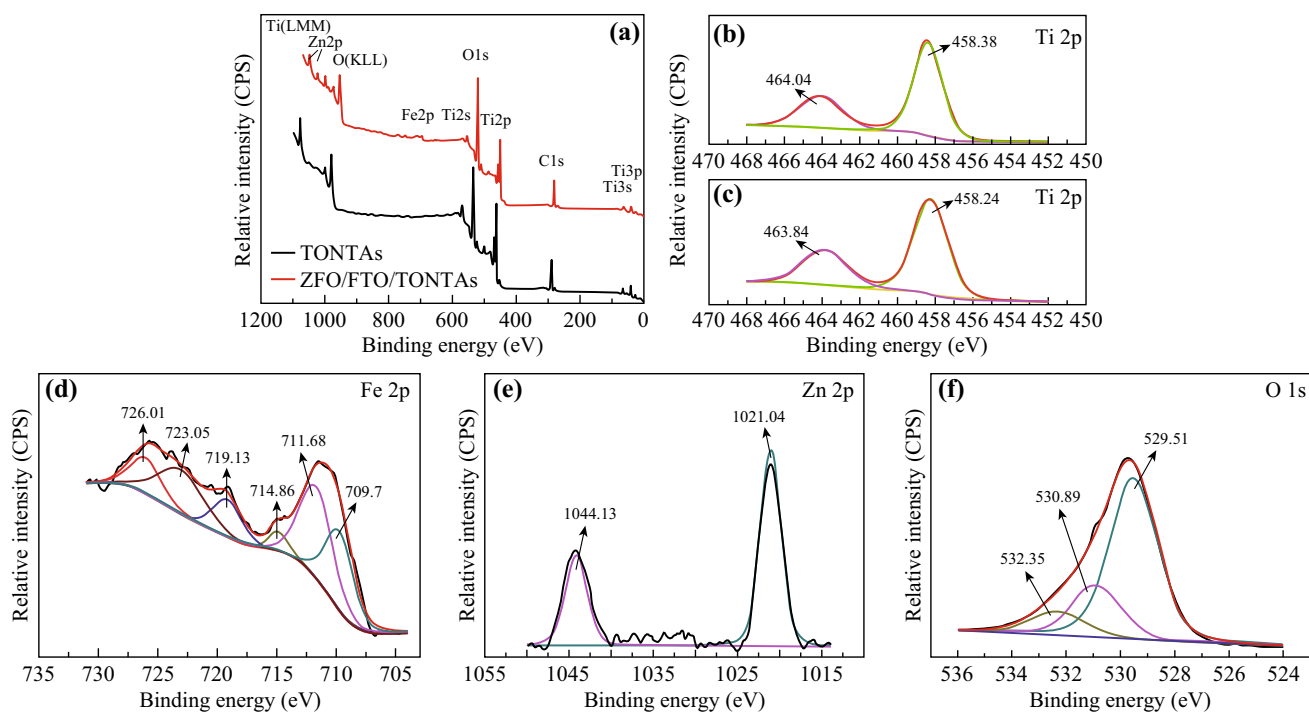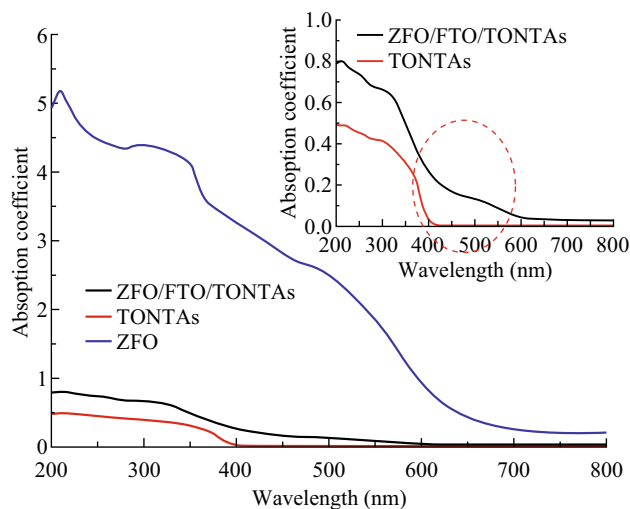
Fig. 4 **a** XPS survey spectra of the TONTAs annealed at 600 °C and ZFO/FTO/TONTAs annealed at 750 °C. Ti 2p core level XPS spectra of: **b** the TONTAs annealed at 600 °C and **c** ZFO/FTO/TONTAs annealed at 750 °C. XPS spectra of the ZFO/FTO/TONTAs annealed at 750 °C: **d** Fe 2p, **e** Zn 2p, and **f** O 1s core level

TONTAs (Fig. 4f) can be fitted with three peaks. These peaks are located at 532.35 eV and are ascribed to the presence of the hydroxyl group from absorbed moisture or oxygen vacancy-related defects. The peaks situated at 529.51 and 530.89 eV correspond to lattice oxygen in TiO_2 and ZFO, respectively [21, 59].

UV–Vis diffuse reflection was used to investigate the optical properties of the ZFO/FTO/TONTAs, and the optical absorbance was calculated from the optical reflectance data using the Kubelka–Munk function $(\alpha = (1 - R)^2/2R)$. Here, α and R are the absorption coefficient and diffuse reflectance coefficient, respectively [62]. As presented in Fig. 5, the ZFO/FTO/TONTAs have a relatively larger α than the annealed TONTAs throughout the UV–Vis wavelength range. Its α is significantly smaller than that of the pure ZFO nanoparticles. The inset of Fig. 5 indicates that visible light (400–760 nm) absorption of the ZFO/FTO/TONTAs is higher than that of the annealed TONTAs. This might be due to the presence of ZFO and FTO in the heterostructured ZFO/FTO/TONTAs.

MB photocatalysis degradation experiments were used to probe the reaction and study the photocatalytic activities of the ZFO/FTO/TONTAs. Figure 6a shows that under simulated sunlight irradiation for 10 min, the ZFO/FTO/TONTAs degrade approximately 41% of MB. About 12% of MB is degraded by the TONTAs, and only 3% of MB degrades in the presence of ZFO under the same

Fig. 5 UV–Vis diffuse absorption spectra of the ZFO nanocrystals: TONTAs annealed at 600 °C and ZFO/FTO/TONTAs annealed at 750 °C. The inset shows the corresponding magnified spectra

conditions. At 40 min of irradiation, the ZFO/FTO/TONTAs could completely degrade the MB molecules. Under the same conditions, the photocatalytic degradation of MB molecules assigned to the TONTAs and ZFO is 51 and 18%, respectively.

The specific surface areas of the ZFO/FTO/TONTAs, TONTAs, and ZFO are 44, 53, and 127.2 m^2 g^{-1},
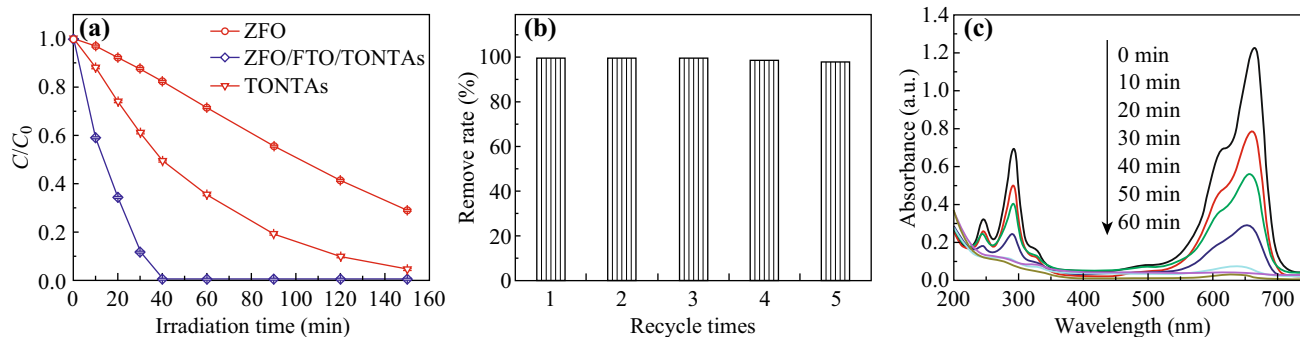
Fig. 6 **a** Photocatalytic degradation of MB vs. the irradiation time under simulated sunlight in the presence of the ZFO nanocrystals, TONTAs annealed at 600 °C, and ZFO/FTO/TONTAs annealed at 750 °C. **b** Recycling test for the ZFO/FTO/TONTAs. **c** UV–Vis absorbance of MB as a function of the irradiation time

respectively. In fact, the photocatalytic degradation of MB is achieved through redox reactions that occur at the interface of the photocatalyst and MB molecules. Thus, the specific surface area is an important parameter of the photocatalyst. Nevertheless, while ZFO has a relatively large α and specific surface area, its photocatalytic degradation of MB is still very slow. To better compare the photocatalytic efficiency of the above samples, a kinetic study of MB degradation was performed using a pseudo-first-order kinetics model:

$$\ln\left(\frac{C_0}{C}\right) = kt \tag{1}$$

where k is the apparent reaction constant (min^{-1}), and C_0 and C are the initial concentration and reaction concentration of MB, respectively. The photocatalytic degradation of MB vs. the irradiation time under simulated sunlight was examined in the presence of the ZFO nanocrystals, TON-TAs annealed at 600 °C, and ZFO/FTO/TONTAs annealed at 750 °C (Fig. 6a), and the k values are 0.0074, 0.0194, and 0.0646 min^{-1}, respectively. These values demonstrate that the ZFO/FTO/TONTAs have a higher efficiency for photocatalytic degradation of MB. Lou et al. reported that the optimal k of FTO/TiO$_2$ hollow nanospheres was approximately 0.1 min^{-1} when they were used for photocatalytic degradation of rhodamine B [63]. In addition, Xu et al. found that the optimal k of a TiO$_2$/ZFO photocatalyst was 0.0018 min^{-1} when they were used for photocatalytic degradation of methyl orange [46]. These degradation rates were obtained in different irradiation environments.

As shown in Fig. 6b, the MB removal rate using the ZFO/FTO/TONTAs exhibits a minor decrease (within 3%) after five cycles, which indicates that the ZFO/FTO/TONTAs could remain active and reliable for long-term use. In Fig. 6c, the UV–Vis absorbance demonstrates that the concentration of MB decreases sharply as a function of the irradiation time, which confirms the degradation of MB.

PL spectra are commonly used to investigate the separation efficiency of photogenerated electron–hole pairs in a semiconductor because recombination of electron–hole pairs produces a PL emission signal [64]. Figure 7a shows that the peaks in the PL spectra (near 489 nm) sharply decrease for the ZFO/FTO/TONTAs with respect to those of ZFO and the TONTAs, which indicates efficient separation of the photogenerated electron–hole pairs. Furthermore, it explains why the ZFO/FTO/TONTAs show higher photocatalytic degradation efficiency. To further prove the effective charge separation of the ZFO/FTO/TONTAs, electrochemical analysis was carried out. The current–time (I-t) characteristics of the TONTA and ZFO/FTO/TONTA electrodes recorded in 0.1 M Na$_2$SO$_4$ under simulated sunlight irradiation are shown in Fig. 7b. The photocurrent density of the ZFO/FTO/TONTAs is much higher than that of the TONTAs, which further confirms that ZFO/FTO/TONTAs have a higher separation efficiency of photogenerated electron–hole pairs.

According to the Kubelka–Munk function and the plot of $(\alpha h\nu)^2$ against the energy of absorbed light ($h\nu$), the bandgaps (E_g) of ZFO and the TONTAs are estimated as 1.85 and 3.16 eV, respectively (Fig. 8). Courtin et al. [50] reported that the E_g of FTO was approximately 2.2 eV. E_{CB} and E_{VB} represent the band edge potentials of the conduction band (CB) and valence band (VB), respectively. These can be calculated from the following equations [65]:

$$E_{CB} = X - E^C - 0.5E_g \tag{2}$$

$$E_{VB} = X - E^C + 0.5E_g \tag{3}$$

where X is the electronegativity of the semiconductor, which is the geometric mean of the electronegativity of the constituent atoms, and E^C is the energy of the free electrons on the hydrogen scale (approximately 4.5 eV). Moreover, the X values for ZFO, FTO, and TiO$_2$ are 5.05, 5.86, and 5.81 eV, respectively [50, 61, 66]. Based on Eqs. 1 and 2, the E_{CB} values of ZFO, FTO, and TiO$_2$ are separately
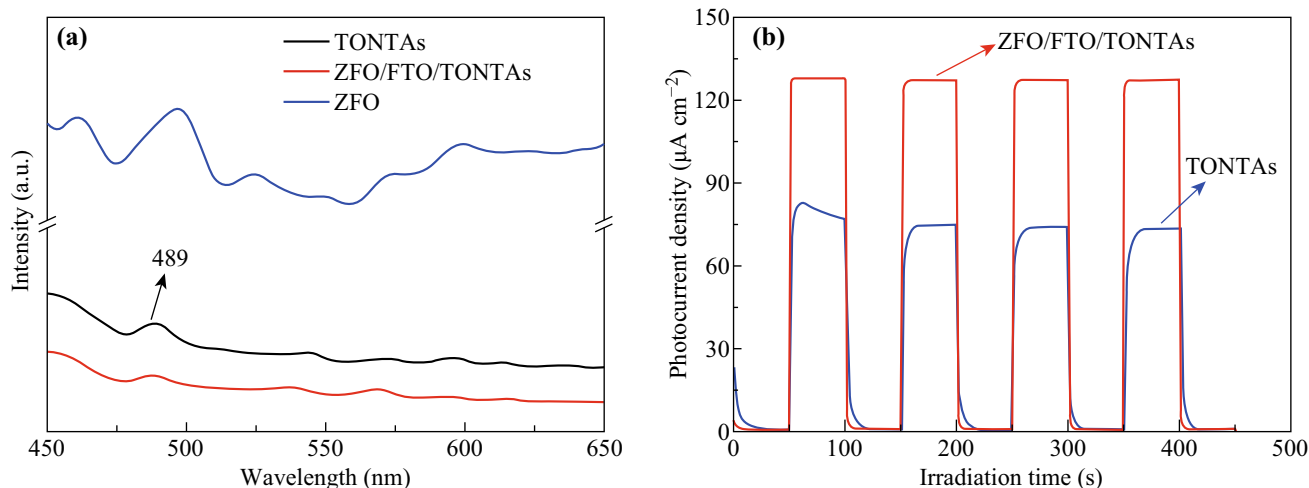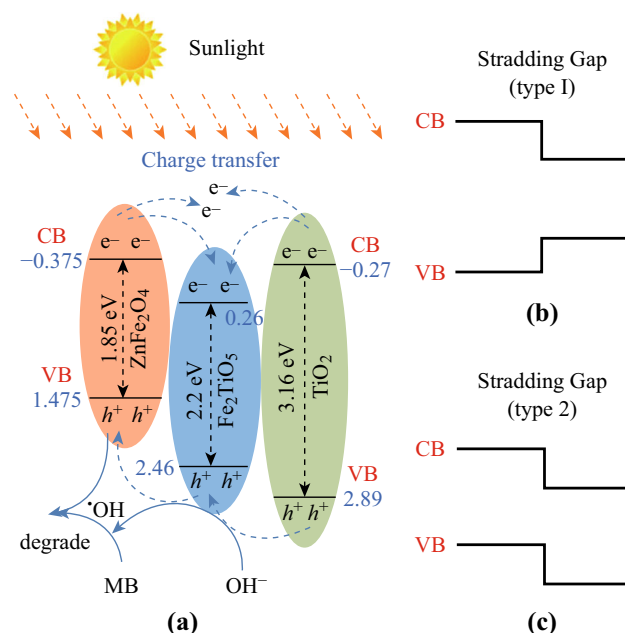
Fig. 7 **a** PL spectra of the ZFO, TONTAs, and ZFO/FTO/TONTAs. **b** Photocurrent responses of the TONTAs and ZFO/FTO/TONTAs under simulated sunlight irradiation in a 0.1 M Na_2SO_4 solution recorded at 1.0 V. The illumination was interrupted every 50 s
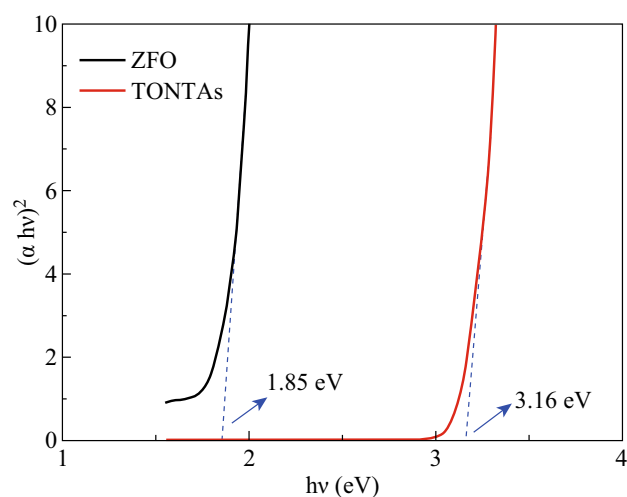
Fig. 8 Plots of $(\alpha h\nu)^2$ versus the incident photon energy that are assigned to the as-prepared ZFO and TONTAs

Fig. 9 Schematic of the energy band structure of **a** the ZFO/FTO/TONTAs heterojunction, **b** type I band alignment, and **c** type II and alignment

estimated to be − 0.375, 0.26, and − 0.27 eV/normal hydrogen electrode (NHE). Their corresponding E_{VB} values are 1.475, 2.46, and 2.89 eV/NHE.

The ZFO/FTO/TONTAs consist of three different semiconductors (ZFO, FTO, and TiO_2), and two different heterojunctions are formed in the ZFO/FTO/TONTAs. As depicted in Fig. 9a, the CB of FTO lies below that of TiO_2 and ZFO, and the VB of ZFO lies above that of FTO and TiO_2. This produces a staggered type II band alignment between ZFO and FTO, while a type I band alignment is produced between FTO and TiO_2. This implies the coexistence of type I and staggered type II band alignments in ZFO/FTO/TONTAs. The photogenerated electrons present in the CB of ZFO at the ZFO/FTO interface—with a staggered type II band alignment—are transferred to the

CB of FTO, while the holes present in the VB of FTO are transferred to the VB of ZFO. This facilitates separation of photogenerated electrons and holes. However, because of formation of type I band alignment at the FTO/TiO_2 interface, the photogenerated electrons present in the CB of TiO_2 are transferred to the CB of FTO, and the holes present in the VB of TiO_2 are also transferred to the VB of FTO. In this case, the photogenerated electrons and holes easily recombine. Nevertheless, the holes that are originally transferred from the VB of TiO_2 to the VB of FTO

can continue to be transferred to the VB of ZFO because there is a ZFO/FTO heterojunction in the ZFO/FTO/TONTAs. Thus, they are reduced, and the photogenerated electrons recombine with holes at the FTO/TiO$_2$ interface.

Lotgering et al. [67] demonstrated the existence of electron exchange between Fe^{2+} and Fe^{3+} via paramagnetic Mossbauer spectroscopy to test Ti-doped ZFO. Figure 4d shows that Fe^{2+} and Fe^{3+} coexist in the ZFO/FTO/TONTAs, and this implies that the photogenerated electrons can be transferred at the ZFO/FTO interface by Fe^{2+}/Fe^{3+} electron exchange. In addition, the unique axially oriented structure of the ZFO/FTO/TONTAs also facilitates electron transfer, supporting the view that the photogenerated electrons and holes can be effectively separated. Furthermore, the holes on the surface of the ZFO could reduce H$_2$O or OH$^-$ to ·OH because its energy (1.475 eV vs. NHE) is higher than the standard redox potential of $E\left(\text{OH}^-/_{\cdot\text{OH}}\right) = 1.99$ eV (vs. NHE). Strongly oxidative ·OH could degrade MB. Thus, the improved photocatalytic degradation efficiency seen in the ZFO/FTO/TONTAs is mainly attributed to the following points: (1) enhanced visible light absorption from the introduction of ZFO and (2) more effective separation of photogenerated electrons and holes because of the coexistence of type I and staggered type II band alignments in the ZFO/FTO/TONTAs.

4 Conclusions

In this work, ZFO nanocrystals were successfully perfused into the TONTA pipelines using a bias voltage-assisted perfusion method. After annealing at 750 °C for 2 h, heterostructured ZFO/FTO/TONTAs were obtained. This formed a staggered type II band alignment at the ZFO/FTO interface and a type I band alignment at the FTO/TiO$_2$ interface. Because of the singular nanoscale heterostructure, the visible light absorption of the ZFO/FTO/TONTAs was greatly enhanced upon introduction of ZFO and FTO. Despite the small specific surface area, the efficiency of the ZFO/FTO/TONTAs in the photocatalytic degradation of MB was significantly improved upon irradiation with simulated sunlight with a reliable recycling ability.

References

1. Q. Li, F. Wang, L. Sun, Z. Jiang, T. Ye, M. Chen, Q. Bai, C. Wang, X. Han, Design and synthesis of Cu@CuS yolk–shell structures with enhanced photocatalytic activity. Nano-Micro Lett. **9**(3), 35 (2017). https://doi.org/10.1007/s40820-017-0135-7

2. X. Zhang, D. Xu, D. Huang, F. Liu, K. Xu, H. Wang, S. Zhang, Enhanced visible-light-driven photocatalytic activities of LiInO$_2$ by Mo^{6+}-doping strategy. J. Am. Ceram. Soc. **100**(7), 2781–2789 (2017). https://doi.org/10.1111/jace.14799

3. X. Han, X. He, F. Wang, J. Chen, J. Xu, X. Wang, X. Han, Engineering an n-doped Cu$_2$O@N–C interface with long-lived photo-generated carriers for efficient photoredox catalysts. J. Mater. Chem. A **5**(21), 10220–10226 (2017). https://doi.org/10.1039/C7TA01909B

4. L. Sun, X. Han, Z. Jiang, T. Ye, R. Li, X. Zhao, X. Han, Fabrication of cubic Zn$_2$SnO$_4$/SnO$_2$ complex hollow structures and their sunlight-driven photocatalytic activity. Nanoscale **8**(26), 12858–12862 (2016). https://doi.org/10.1039/C5NR08004E

5. Y.J. Gu, Y.J. Su, D. Chen, H.J. Geng, Z.L. Li, L.Y. Zhang, Y.F. Zhang, Hydrothermal synthesis of hexagonal CuSe nanoflakes with excellent sunlight-driven photocatalytic activity. CrystEngComm **16**, 9185–9190 (2014). https://doi.org/10.1039/c4ce01470g

6. K. Zhu, N.R. Neale, A. Miedaner, A.J. Frank, Enhanced charge-collection efficiencies and light scattering in dye-sensitized solar cells using oriented TiO$_2$ nanotubes arrays. Nano Lett. **7**(1), 69–74 (2007). https://doi.org/10.1021/nl062000o

7. M.Z. Ge, S.H. Li, J.Y. Huang, K.Q. Zhang, S.S. Al-Deyab, Y.K. Lai, TiO$_2$ nanotube arrays loaded with reduced graphene oxide films: facile hybridization and promising photocatalytic application. J. Mater. Chem. A **3**(7), 3491–3499 (2015). https://doi.org/10.1039/C4TA06354F

8. I.S. Cho, J. Choi, K. Zhang, S.J. Kim, M.J. Jeong, L.L. Cai, T. Park, X.L. Zheng, J.H. Park, Highly efficient solar water splitting from transferred TiO$_2$ nanotube arrays. Nano Lett. **15**(9), 5709–5715 (2015). https://doi.org/10.1021/acs.nanolett.5b01406

9. S.Z. Liang, J.F. He, Z.H. Sun, Q.H. Liu, Y. Jiang, H. Cheng, B. He, Z. Xie, S.Q. Wei, Improving photoelectrochemical water splitting activity of TiO$_2$ nanotube arrays by tuning geometrical parameters. J. Phys. Chem. C **116**(16), 9049–9053 (2012). https://doi.org/10.1021/jp300552s

10. J.S. Yang, W.P. Liao, J.J. Wu, Morphology and interfacial energetics controls for hierarchical anatase/rutile TiO$_2$ nanostructured array for efficient photoelectrochemical water splitting. ACS Appl. Mater. Interfaces **5**(15), 7425–7431 (2013). https://doi.org/10.1021/am401746b

11. M.Z. Ge, C.Y. Cao, J.Y. Huang, S.H. Li, Z. Chen, K.Q. Zhang, S.S. Al-Deyabd, Y.K. Lai, A review of one-dimensional TiO$_2$ nanostructured materials for environmental and energy applications. J. Mater. Chem. A **4**(18), 6772–6801 (2016). https://doi.org/10.1039/C5TA09323F

12. X.L. He, Y.Y. Cai, H.M. Zhang, C.H. Liang, Photocatalytic degradation of organic pollutants with ag decorated free-standing TiO$_2$ nanotube arrays and interface electrochemical response.

J. Mater. Chem. **21**(2), 475–480 (2011). https://doi.org/10.1039/C0JM02404J

13. Z.Y. Liu, X.T. Zhang, S. Nishimoto, T. Murakami, A. Fujishima, Efficient photocatalytic degradation of gaseous acetaldehyde by highly ordered TiO_2 nanotube arrays. Environ. Sci. Technol. **42**(22), 8547–8551 (2008). https://doi.org/10.1021/es8016842

14. J. Choi, S. Song, G. Kang, T. Park, Dye-sensitized solar cells employing doubly or singly open-ended TiO_2 nanotube arrays: structural geometry and charge transport. ACS Appl. Mater. Interfaces **6**(17), 15388–15394 (2014). https://doi.org/10.1021/am503934s

15. X.F. Gao, D.S. Guan, J.W. Huo, J.H. Chen, C. Yuan, Free standing TiO_2 nanotube array electrodes with an ultra-thin Al_2O_3 barrier layer and ticl4 surface modification for highly efficient dye sensitized solar cells. Nanoscale **5**(21), 10438–10446 (2013). https://doi.org/10.1039/c3nr03198e

16. D. Kuang, J. Brillet, P. Chen, M. Takata, S. Uchida, H. Miura, K. Sumioka, S.M. Zakeeruddin, M. Gratzel, Application of highly ordered TiO_2 nanotube arrays in flexible dye-sensitized solar cells. ACS Nano **2**(6), 1113–1116 (2008). https://doi.org/10.1021/nn800174y

17. C.K. Xu, P.H. Shin, L.L. Cao, J.M. Wu, D. Gao, Ordered TiO_2 nanotube arrays on transparent conductive oxide for dye-sensitized solar cells. Chem. Mater. **22**(1), 143–148 (2010). https://doi.org/10.1021/cm9027513

18. P.T. Sheng, W.L. Li, J. Cai, X. Wang, X. Tong, Q.Y. Cai, C.A. Grimes, A novel method for the preparation of a photocorrosion stable core/shell cdte/cds quantum dot TiO_2 nanotube array photoelectrode demonstrating an am 1.5 g photoconversion efficiency of 6.12%. J. Mater. Chem. A **1**(26), 7806–7815 (2013). https://doi.org/10.1039/c3ta10255f

19. C.Y. Zhai, M.S. Zhu, Y.T. Lu, F.F. Ren, C.Q. Wang, Y.K. Du, P. Yang, Reduced graphene oxide modified highly ordered TiO_2 nanotube arrays photoelectrode with enhanced photoelectrocatalytic performance under visible-light irradiation. Phys. Chem. Chem. Phys. **16**(28), 14800–14807 (2014). https://doi.org/10.1039/C4CP01401D

20. J. Zhang, J.H. Bang, C.C. Tang, P.V. Kamat, Tailored TiO_2–$SrTiO_3$ heterostructure nanotube arrays for improved photoelectrochemical performance. ACS Nano **4**(1), 387–395 (2010). https://doi.org/10.1021/nn901087c

21. Y. Hou, X.Y. Li, Q.D. Zhao, X. Quan, G.H. Chen, Electrochemical method for synthesis of a $ZnFe_2O_4$/TiO_2 composite nanotube array modified electrode with enhanced photoelectrochemical activity. Adv. Funct. Mater. **20**(13), 2165–2174 (2010). https://doi.org/10.1002/adfm.200902390

22. Z.C. Lian, W.C. Wang, S.N. Xiao, X. Li, Y.Y. Cui, D.Q. Zhang, G.S. Li, H.X. Li, Plasmonic silver quantum dots coupled with hierarchical TiO_2 nanotube arrays photoelectrodes for efficient visible-light photoelectrocatalytic hydrogen evolution. Sci. Rep. **5**, 10461 (2015). https://doi.org/10.1038/srep10461

23. L.S. Hu, C.C. Fong, X.M. Zhang, L.L. Chan, P.K.S. Lam, P.K. Chu, K.Y. Wong, M.S. Yang, Au nanoparticles decorated TiO_2 nanotube arrays as a recyclable sensor for photoenhanced electrochemical detection of bisphenol A. Environ. Sci. Technol. **50**(8), 4430–4438 (2016). https://doi.org/10.1021/acs.est.5b05857

24. Z.H. Zhang, L.B. Zhang, M.N. Hedhili, H.N. Zhang, P. Wang, Plasmonic gold nanocrystals coupled with photonic crystal seamlessly on TiO_2 nanotube photoelectrodes for efficient visible light photoelectrochemical water splitting. Nano Lett. **13**(1), 14–20 (2013). https://doi.org/10.1021/nl3029202

25. M.D. Ye, J.J. Gong, Y.K. Lai, C.J. Lin, Z.Q. Lin, High-efficiency photoelectrocatalytic hydrogen generation enabled by palladium quantum dots-sensitized TiO_2 nanotube arrays. J. Am. Chem. Soc. **134**(38), 15720–15723 (2012). https://doi.org/10.1021/ja307449z

26. S.A. Ansari, M.M. Khan, M.O. Ansaric, M.H. Cho, Nitrogen-doped titanium dioxide (n-doped TiO_2) for visible light photocatalysis. New J. Chem. **40**(4), 3000–3009 (2016). https://doi.org/10.1039/C5NJ03478G

27. J.L. Zhang, Y.M. Wu, M.Y. Xing, S.A.K. Leghari, S. Sajjad, Development of modified n doped TiO_2 photocatalyst with metals, nonmetals and metal oxides. Energy Environ. Sci. **3**(6), 715–726 (2010). https://doi.org/10.1039/b927575d

28. Q.F. Chen, H.J. Shi, W.M. Shi, Y. Xu, D. Wu, Enhanced visible photocatalytic activity of titania-silica photocatalysts: effect of carbon and silver doping. Catal. Sci. Technol. **2**(6), 1213–1220 (2012). https://doi.org/10.1039/c2cy00545j

29. D.Y. Qi, M.Y. Xing, J.L. Zhang, Hydrophobic carbon-doped TiO_2/MCF-F composite as a high performance photocatalyst. J. Phys. Chem. C **118**(14), 7329–7336 (2014). https://doi.org/10.1021/jp4123979

30. W. Ho, J.C. Yu, S. Lee, Synthesis of hierarchical nanoporous f-doped TiO_2 spheres with visible light photocatalytic activity. Chem. Commun. **111**(10), 1115–1117 (2006). https://doi.org/10.1039/b515513d

31. K.L. Lv, B. Cheng, J.G. Yu, G. Liu, Fluorine ions-mediated morphology control of anatase TiO_2 with enhanced photocatalytic activity. Phys. Chem. Chem. Phys. **14**(16), 5349–5362 (2012). https://doi.org/10.1039/c2cp23461k

32. G.S. Wu, J.P. Wang, D.F. Thomas, A.C. Chen, Synthesis of f-doped flower-like TiO_2 nanostructures with high photoelectrochemical activity. Langmuir **24**(7), 3503–3509 (2008). https://doi.org/10.1021/la703098g

33. S. In, A. Orlov, R. Berg, F. Garcia, S. Pedrosa-Jimenez, M.S. Tikhov, D.S. Wright, R.M. Lambert, Effective visible light-activated B-doped and B, N-codoped TiO_2 photocatalysts. J. Am. Chem. Soc. **129**(45), 13790–13791 (2007). https://doi.org/10.1021/ja0749237

34. H.J. Tian, L.H. Hu, C.N. Zhang, S.H. Chen, J.A. Sheng, L. Mo, W.Q. Liu, S.Y. Dai, Enhanced photovoltaic performance of dye-sensitized solar cells using a highly crystallized mesoporous TiO_2 electrode modified by boron doping. J. Mater. Chem. **21**(3), 863–868 (2011). https://doi.org/10.1039/C0JM02941F

35. S.C. Han, Y.C. Pu, L.X. Zheng, J.Z. Zhang, X.S. Fang, Shell-thickness dependent electron transfer and relaxation in type-ii core-shell CdS/TiO_2 structures with optimized photoelectrochemical performance. J. Mater. Chem. A **3**(45), 22627–22635 (2015). https://doi.org/10.1039/C5TA07100C

36. G.S. Li, L. Wu, F. Li, P.P. Xu, D.Q. Zhang, H.X. Li, Photoelectrocatalytic degradation of organic pollutants via a cds quantum dots enhanced TiO_2 nanotube array electrode under visible light irradiation. Nanoscale **5**(5), 2118–2125 (2013). https://doi.org/10.1039/c3nr34253k

37. W.T. Sun, Y. Yu, H.Y. Pan, X.F. Gao, Q. Chen, L.M. Peng, CdS quantum dots sensitized TiO_2 nanotube-array photoelectrodes. J. Am. Chem. Soc. **130**(4), 1124–1125 (2008). https://doi.org/10.1021/ja0777741

38. J.Y. Kim, S.B. Choi, J.H. Noh, S. HunYoon, S. Lee, T.H. Noh, A.J. Frank, K.S. Hong, Synthesis of CdSe-TiO_2 nanocomposites and their applications to TiO_2 sensitized solar cells. Langmuir **25**(9), 5348–5351 (2009). https://doi.org/10.1021/la804310z

39. B. Vercelli, G. Zotti, A. Berlin, M. Pasini, C. Botta, R. Gerbasi, T.L. Nelson, R.D. McCullough, Oligo(poly)thiophene sensitization of cdse nanocrystal and TiO_2 polycrystalline electrodes: a photoelectrochemical investigation. J. Phys. Chem. C **116**(2), 2033–2039 (2012). https://doi.org/10.1021/jp209042c

40. S.J. Kim, Y.K. Cho, J. Seok, N.S. Lee, B. Son et al., Highly branched RuO_2 nanoneedles on electrospun TiO_2 nanofibers as an efficient electrocatalytic platform. ACS Appl. Mater. Interfaces

7(28), 15321–15330 (2015). https://doi.org/10.1021/acsami.5b03178

41. M.T. Uddin, Y. Nicolas, C. Olivier, T. Toupance, M.M. Muller et al., Preparation of RuO_2/TiO_2 mesoporous heterostructures and rationalization of their enhanced photocatalytic properties by band alignment investigations. J. Phys. Chem. C **117**(42), 22098–22110 (2013). https://doi.org/10.1021/jp407539c

42. J.H. Kim, K. Zhu, Y.F. Yan, C.L. Perkins, A.J. Frank, Microstructure and pseudocapacitive properties of electrodes constructed of oriented $NiO–TiO_2$ nanotube arrays. Nano Lett. **10**(10), 4099–4104 (2010). https://doi.org/10.1021/nl102203s

43. K. Nakamura, T. Oshikiri, K. Ueno, Y.M. Wang, Y. Kamata, Y. Kotake, H. Misawa, Properties of plasmon-induced photoelectric conversion on a TiO_2/NiO p-n junction with au nanoparticles. J. Phys. Chem. Lett. **7**(6), 1004–1009 (2016). https://doi.org/10.1021/acs.jpclett.6b00291

44. G.L. Fan, J. Tong, F. Li, Visible-light-induced photocatalyst based on cobalt-doped zinc ferrite nanocrystals. Ind. Eng. Chem. Res. **51**(42), 13639–13647 (2012). https://doi.org/10.1021/ie201933g

45. A. Meidanchi, O. Akhavan, Superparamagnetic zinc ferrite spinel-graphene nanostructures for fast wastewater purification. Carbon **69**, 230–238 (2014). https://doi.org/10.1016/j.carbon.2013.12.019

46. S.H. Xu, D.L. Feng, W.F. Shangguan, Preparations and photocatalytic properties of visible-light-active zinc ferrite-doped TiO_2 photocatalyst. J. Phys. Chem. C **113**(6), 2463–2467 (2009). https://doi.org/10.1021/jp806704y

47. L. Chen, S. Li, Z. Liu, Y. Lu, D. Wang, Y. Lin, T. Xie, Surface photovoltage phase spectra for analysing the photogenerated charge transfer and photocatalytic activity of $ZnFe_2O_4–TiO_2$ nanotube arrays. Phys. Chem. Chem. Phys. **15**(34), 14262–14269 (2013). https://doi.org/10.1039/c3cp51850g

48. A. Sarkar, A.K. Singh, D. Sarkar, G.G. Khan, K. Mandal, Three-dimensional nanoarchitecture of $BiFeO_3$ anchored TiO_2 nanotube arrays for electrochemical energy storage and solar energy conversion. ACS Sustain. Chem. Eng. **3**(9), 2254–2263 (2015). https://doi.org/10.1021/acssuschemeng.5b00519

49. C.L. Zhu, H.L. Yu, Y. Zhang, T.S. Wang, Q.Y. Ouyang, L.H. Qi, Y.J. Chen, X.Y. Xue, Fe_2O_3/TiO_2 tube-like nanostructures: synthesis, structural transformation and the enhanced sensing properties. ACS Appl. Mater. Interfaces **4**(2), 665–671 (2012). https://doi.org/10.1021/am201689x

50. E. Courtin, G. Baldinozzi, M.T. Sougrati, L. Stievano, C. Sanchez, C. Laberty-Robert, New Fe_2TiO_5-based nanoheterostructured mesoporous photoanodes with improved visible light photoresponses. J. Mater. Chem. A **2**(18), 6567–6577 (2014). https://doi.org/10.1039/C4TA00102H

51. Q.H. Liu, J.F. He, T. Yao, Z.H. Sun, W.R. Cheng et al., Aligned Fe_2TiO_5-containing nanotube arrays with low onset potential for visible-light water oxidation. Nat. Commun. **5**(5), 5122 (2014). https://doi.org/10.1038/ncomms6122

52. X.Q. Wang, L. Chen, Q.B. Fan, J.X. Fan, G.L. Xu, M.H. Yan, M.J. Henderson, J. Courtois, K. Xiong, Lactoferrin-assisted synthesis of zinc ferrite nanocrystal: its magnetic performance and photocatalytic activity. J. Alloys Compd. **652**, 132–138 (2015). https://doi.org/10.1016/j.jallcom.2015.08.228

53. O. Carp, C.L. Huisman, A. Reller, Photoinduced reactivity of titanium dioxide. Prog. Solid State Chem. **32**(1–2), 33–177 (2004). https://doi.org/10.1016/j.progsolidstchem.2004.08.001

54. D. Tsukamoto, Y. Shiraishi, Y. Sugano, S. Ichikawa, S. Tanaka, T. Hirai, Gold nanoparticles located at the interface of anatase/rutile TiO_2 particles as active plasmonic photocatalysts for aerobic oxidation. J. Am. Chem. Soc. **134**(14), 6309–6315 (2012). https://doi.org/10.1021/ja2120647

55. Y. Liu, Y. Luo, A.A. Elzatahry, W. Luo, R. Che et al., Mesoporous TiO_2 mesocrystals: remarkable defects-induced crystallite-interface reactivity and their in situ conversion to single crystals. ACS Cent. Sci. **1**(7), 400–408 (2015). https://doi.org/10.1021/acscentsci.5b00256

56. B. Santara, P.K. Giri, K. Imakita, M. Fujii, Evidence of oxygen vacancy induced room temperature ferromagnetism in solvothermally synthesized undoped TiO_2 nanoribbons. Nanoscale **5**(12), 5476–5488 (2013). https://doi.org/10.1039/c3nr00799e

57. F. Zuo, L. Wang, T. Wu, Z.Y. Zhang, D. Borchardt, P.Y. Feng, Self-doped Ti^{3+} enhanced photocatalyst for hydrogen production under visible light. J. Am. Chem. Soc. **132**(34), 11856–11857 (2010). https://doi.org/10.1021/ja103843d

58. H. Gupta, P. Paul, N. Kumar, S. Baxi, D.P. Das, One pot synthesis of water-dispersible dehydroascorbic acid coated Fe_3O_4 nanoparticles under atmospheric air: blood cell compatibility and enhanced magnetic resonance imaging. J. Colloid Interface Sci. **430**, 221–228 (2014). https://doi.org/10.1016/j.jcis.2014.05.043

59. Z.H. Wang, M. Chen, J.X. Shu, Y. Li, One-step solvothermal synthesis of $Fe_3O_4@Cu@Cu_2O$ nanocomposite as magnetically recyclable mimetic peroxidase. J. Alloys Compd. **682**, 432–440 (2016). https://doi.org/10.1016/j.jallcom.2016.04.269

60. C. Frandsen, S. Morup, S.A. McEnroe, P. Robinson, F. Langenhorst, Magnetic phases in hemo-ilmenite: insight from low-velocity and high-field Mossbauer spectroscopy. Geophys. Res. Lett. **34**(7), L07306 (2007). https://doi.org/10.1029/2006GL029063

61. X.J. Chen, Y.Z. Dai, J. Guo, T.H. Liu, X.Y. Wang, Novel magnetically separable reduced graphene oxide (RGO)/$ZnFe_2O_4$/Ag_3PO_4 nanocomposites for enhanced photocatalytic performance toward 2,4-dichlorophenol under visible light. Ind. Eng. Chem. Res. **55**(3), 568–578 (2016). https://doi.org/10.1021/acs.iecr.5b03690

62. Q. Li, R.C. Xie, Y.W. Ll, E.A. Mintz, J.K. Shang, Enhanced visible-light-induced photocatalytic disinfection of e-coli by carbon-sensitized nitrogen-doped titanium oxide. Environ. Sci. Technol. **41**(14), 5050–5056 (2007). https://doi.org/10.1021/es062753c

63. Z. Lou, Y. Li, H. Song, Z. Ye, L. Zhu, Fabrication of Fe_2TiO_5/TiO_2 nanoheterostructures with enhanced visible-light photocatalytic activity. RSC Adv. **6**(51), 45343–45348 (2016). https://doi.org/10.1039/C6RA06763H

64. H. Song, L. Zhu, Y. Li, Z. Lou, M. Xiao, Z. Ye, Preparation of $ZnFe_2O_4$ nanostructures and highly efficient visible-light-driven hydrogen generation with the assistance of nanoheterostructures. J. Mater. Chem. A **3**(16), 8353–8360 (2015). https://doi.org/10.1039/C5TA00737B

65. X.J. Guan, L.J. Guo, Cocatalytic effect of $SrTiO_3$ on Ag_3PO_4 toward enhanced photocatalytic water oxidation. ACS Catal. **4**(9), 3020–3026 (2014). https://doi.org/10.1021/cs5005079

66. S.Y. Cao, X.Q. Yan, Z. Kang, Q.J. Liang, X.Q. Liao, Y. Zhang, Band alignment engineering for improved performance and stability of $ZnFe_2O_4$ modified CdS/ZnO nanostructured photoanode for pec water splitting. Nano Energy **24**, 25–31 (2016). https://doi.org/10.1016/j.nanoen.2016.04.001

67. F.K. Lotgering, A.M. Van Diepen, Electron exchange between Fe^{2+} and Fe^{3+} ions on octahedral sites in spinels studied by means of paramagnetic Mössbauer spectra and susceptibility measurements. J. Phys. Chem. Solids **38**(6), 565–572 (1977). https://doi.org/10.1016/0038-1098(77)90861-4

Springer